Eur. Phys. J. C (2024) 84:354
https://doi.org/10.1140/epjc/s10052-024-12541-y

THE EUROPEAN PHYSICAL JOURNAL C

Regular Article - Theoretical Physics

Sensitivity to CP discovery in the presence of Lorentz invariance-violating potential at T2HK/T2HKK

Supriya Pan[1,2,a], **Kaustav Chakraborty**[1,b], **Srubabati Goswami**[1,3,c]

[1] Physical Research Laboratory, Ahmedabad, Gujarat 380009, India
[2] Indian Institute of Technology, Gandhinagar, Gujarat 382355, India
[3] Department of Physics and Astronomy, Northwestern University, Evanston, IL 60208, USA

Received: 22 September 2023 / Accepted: 11 February 2024

Abstract The investigation of conservation/violation of conjugation and parity (CP) symmetry in the leptonic sector is essential to understanding the evolution of the universe. Lorentz invariance and CPT are fundamental symmetries of nature. The violation of Lorentz invariance can also lead to CPT violations. The standard three-flavor neutrino oscillation framework presents a scenario for observing the signature of Lorentz invariance and CP violations. This work focuses on the effect of Lorentz invariance-violating parameters on the sensitivity to CP violation. We investigate the sensitivity in two proposed configurations of the upcoming T2HK experiment: (i) one detector each placed at 295 km and 1100 km, and (ii) two identical detectors at 295 km. This study probes the effect of CPT-violating parameters $a_{e\mu}, a_{e\tau}, a_{\mu\tau}$.

1 Introduction

The standard model (SM) of particle physics describes the elementary particles and their interactions, except gravity. The effectiveness of the SM has been thoroughly and successfully tested over the years. However, there have been a few shortcomings that must be addressed. Neutrino oscillation is one phenomenon in which there is inter-conversion among three flavors $\nu_e, \nu_\mu, and \nu_\tau$. This can occur only if the neutrinos are massive. However, in the SM, neutrinos are massless particles. Incorporation of neutrino mass requires some new physics beyond the standard model (BSM). The scale of new physics may be at a higher energy scale, and the standard model can be regarded as an effective low-energy version of the high-energy theory.

The parameters of the three-neutrino oscillation framework include mixing angles $\theta_{12}, \theta_{13}, \theta_{23}$ and Dirac CP phase δ_{13} along with the two mass squared differences $\Delta_{31} = m_3^2 - m_1^2, \Delta_{21} = m_2^2 - m_1^2$ corresponding to mass eigenstates m_1, m_2, m_3. Most of these parameters have been determined by the oscillation experiments [1]. However, the octant of θ_{23}, the CP phase δ_{13}, and the sign of atmospheric mass squared difference Δ_{31} are yet to be precisely determined. Several future experiments with enhanced capabilities are in the pipeline to measure these parameters with increased precision. They also open up the possibility of testing different BSM scenarios. Probing new physics beyond the standard model, including sterile neutrinos, nonstandard interactions, neutrino decay, long-range forces, CPT, and Lorentz invariance violations, in these experiments is currently a very active area of research in neutrino physics.

In this work, the new physics that we focus on is the CPT non-conserving Lorentz invariance violation (LIV). The local relativistic quantum field theories form the basic structure of nature. The primary assumptions of this theory consist of Lorentz invariance and locality of the interactions, along with the hermicity of the Hamiltonian. The conservation of CPT symmetry is embedded in these assumptions. A spontaneous violation of CPT will always be associated with LIV but not vice versa. Since both CPT and Lorentz invariance are fundamental symmetries of nature, any violation will provide us with an indication of new physics governing the laws of nature.

Lorentz invariance protects the isotropy and homogeneity of the local relativistic quantum field theory (QFT) in spacetime. In the minimal $SU(3) \times SU(2) \times U(1)$ SM, this symmetry is conserved. However, there are higher-dimensional theories (related to the Planck scale $\sim 10^{19}$ GeV) where

[a] e-mail: supriyapan@prl.res.in (corresponding author)
[b] e-mail: kaustav.chk@gmail.com
[c] e-mail: sruba@prl.res.in

Published online: 03 April 2024

LIV is generated spontaneously [2–7]. String theories can give rise to the spontaneous breaking of Lorentz symmetry [2–5]. At the level of the standard model, LIV can be manifested as a new physics effect suppressed by the Planck scale. There is also a proposed effective field theoretical description, as given in Ref. [6], that will be consistent with the known physics phenomena of the SM at low energy. The violation of Lorentz invariance and CPT have been tested using kaons [8,9], neutral B_d or B_s mesons [9,10], and neutral D mesons [9,11]. It has also been realized that neutrino oscillation experiments can provide a testing ground for probing signatures of LIV, and there have been several studies on the implications of LIV for various experiments [12–19].

The presence of LIV will also modify the standard neutrino oscillation probabilities, and this can impact the determination of the standard 3ν parameters in future neutrino oscillation experiments. This aspect and the constraints on the LIV parameters have been investigated in several recent works in the context of accelerator and atmospheric neutrino experiments. In Ref. [20], a study was performed to determine bounds on LIV parameters using the iron calorimeter detector at the India-based Neutrino Observatory (INO-ICAL), T2HK (Tokai-to-Hyper-Kamiokande), and the Deep Underground Neutrino Experiment (DUNE). A study on the effect of LIV parameters in NOνA and T2K was reported in Ref. [21]. Efforts have been made to separately understand the effects of LIV interactions and nonstandard interactions (NSIs) at long baseline experiments in [22,23]. Other recent studies related to CPT violation and LIV interactions in neutrinos can be found in [18,24–31].

In our study, we focus on the effects of CPT-violating LIV parameters on the determination of the CP phase in the upcoming T2HK [32]/T2HKK (Tokai-to-Hyper-Kamiokande and Korea) [33] detector. T2HK plans to have two detectors at baseline of 295 km (first oscillation maxima), and T2HKK is proposed to have one detector each at 295 km and 1100 km (second oscillation maxima). We compare and contrast the CP sensitivities in the presence of LIV at both these baselines and explore the synergistic effect between the first and second oscillation maxima.

The remainder of the paper is structured as follows. First, the formalism of LIV in the neutrino sector is described in Sect. 2. This is followed by a discussion on the dependence of the neutrino oscillation probabilities on LIV parameters in Sect. 3. The numerical analysis for CP discovery in the presence of non-diagonal CPT-violating LIV parameters is presented in Sect. 4. In Sect. 5, the precision of the LIV parameters is discussed. Finally, we conclude in Sect. 6.

2 Theory of Lorentz invariance violation

Lorentz invariance violation (LIV) can be comprehended through a standard model extension (SME) framework in the context of a low-energy effective theory [34]. The neutrino behavior is contained in the following Lagrangian:

$$\mathcal{L} = \frac{1}{2}\iota\bar{L}_a\gamma^\mu\overleftrightarrow{D_\mu}L_a - (a_L)_{\mu ab}\bar{L}_a\gamma^\mu L_b + \frac{1}{2}(c_L)_{\mu\nu ab}\bar{L}_a\gamma^\mu\overleftrightarrow{D^\nu}L_b \tag{1}$$

where the first term is the usual standard model kinetic term for the left-handed doublets L_a with index a ranging over the three generations e, μ, τ. The coefficients for Lorentz violation are $(a_L)_{\mu ab}$, which has mass dimension one and controls the CPT violation, and $(c_L)_{\mu\nu ab}$ which is dimensionless and is CPT-conserving. The Lorentz-violating terms in Eq. (1) modify both interactions and propagation of neutrinos. Any interaction effects are expected to be tiny and well beyond the existing sensitivities. In contrast, propagation effects can be substantial if the neutrinos travel large distances. The time evolution of neutrino states is controlled by the effective Hamiltonian extracted from Eq. (1) as

$$(\mathcal{H}_{\text{eff}})_{ab} = E\delta_{ab} + \frac{m^2_{ab}}{2E} + \frac{1}{E}\left(a^\mu_L p_\mu - c^{\mu\nu}_L p_\mu p_\nu\right)_{ab} \tag{2}$$

The LIV-induced parameter a^μ_L (CPT-violating) will change the sign in case of anti-neutrinos, while $c^{\mu\nu}_L$ will remain unchanged. Here, we will focus on only the isotropic component of these parameters in the Sun-centered celestial–equatorial frame and fix μ, ν to be zero and redefine $(a_L)^0_{ab} \equiv a_{ab}$, $(c_L)^{00}_{ab} \equiv c_{ab}$. The Hamiltonian due to LIV is given by

$$H_{\text{LIV}} = \begin{bmatrix} a_{ee} & a_{e\mu} & a_{e\tau} \\ a^\star_{e\mu} & a_{\mu\mu} & a_{\mu\tau} \\ a^\star_{e\tau} & a^\star_{\mu\tau} & a_{\tau\tau} \end{bmatrix} - \frac{4}{3}E\begin{bmatrix} c_{ee} & c_{e\mu} & c_{e\tau} \\ c^\star_{e\mu} & c_{\mu\mu} & c_{\mu\tau} \\ c^\star_{e\tau} & c^\star_{\mu\tau} & c_{\tau\tau} \end{bmatrix} \tag{3}$$

The total Hamiltonian for neutrino propagation, including the standard (Mikheyev–Smirnov–Wolfenstein (MSW) matter effect, is given by

$$H_{\text{tot}} = \frac{1}{2E}\begin{pmatrix} m^2_1 & 0 & 0 \\ 0 & m^2_2 & 0 \\ 0 & 0 & m^2_3 \end{pmatrix} + \begin{pmatrix} \sqrt{2}G_F N_e & 0 & 0 \\ 0 & 0 & 0 \\ 0 & 0 & 0 \end{pmatrix} + H_{\text{LIV}} \tag{4}$$

Here, we only consider CPT-violating LIV parameters $a_{\alpha\beta}$. The non-diagonal parameters are complex and given by $a_{\alpha\beta} = |a_{\alpha\beta}|e^{\iota\phi_{\alpha\beta}}$, whereas diagonal parameters $a_{\alpha\alpha}$ are real. There is an established correlation between CPT-violating LIV parameters and matter -violating parameters given by

Table 1 The table depicts 95% confidence level bounds of CPT-violating non-diagonal LIV parameters from SK and IceCube experiments

Parameter	SK bound	IceCube bound
$a_{e\mu}$	1.8×10^{-23} GeV	N.A.
$a_{e\tau}$	4.1×10^{-23} GeV	N.A.
$a_{\mu\tau}$	0.65×10^{-23} GeV	0.29×10^{-23} GeV

$$\epsilon^m_{\alpha\beta} \equiv \frac{a_{\alpha\beta}}{\sqrt{2}G_F N_e} \tag{5}$$

Irrespective of this mapping, their origins as well as their implications are very different. For example, matter NSIs have similar effects as the MSW matter potential in neutrino propagation, whereas CPT-violating LIV has an intrinsic effect on neutrino propagation even in vacuum [35]. The current constraints on the CPT-violating LIV parameters are given below in Table 1 [36–38].

3 Probabilities in the presence of LIV parameters

In our study, we probe the effects of the CPT-violating LIV parameters $a_{e\mu}$, $a_{e\tau}$, and $a_{\mu\tau}$ on the discovery of the CP phase. For the scope of this work, we use the proposed long baseline experiment configuration of Tokai-to-hyper-Kamiokande (T2HK) and Tokai-to-hyper-Kamiokande and Korea (T2HKK). The setup of T2HKK provides an advantage of two detectors; one at the Hyper Kamiokande site, 295 km away from the source, and another at 1100 km away from the source. At the leading order of $\alpha = \Delta_{21}/\Delta_{31}$, the appearance probability $P_{\mu e}$ depends only on parameters $a_{e\mu}$, $a_{e\tau}$, $\phi_{e\mu}$, and $\phi_{e\tau}$, whereas the disappearance probability depends on $a_{e\mu}$, $a_{e\tau}$, $\phi_{e\mu}$, and $\phi_{e\tau}$. The probabilities are calculated in Refs. [39,40] as follows:

$$P_{\mu e} = P^{3\nu}_{\mu e} + P^{a_{e\mu}}_{\mu e} + P^{a_{e\tau}}_{\mu e} \tag{6}$$

$$P_{\mu\mu} = P^{3\nu}_{\mu\mu} + P^{a_{\mu\tau}}_{\mu\mu}, \tag{7}$$

where $P^{3\nu}_{\mu e}$, $P^{3\nu}_{\mu\mu}$ are the three flavor oscillation probabilities in the matter, and $P^{a_{e\mu}}_{\mu e}$, $P^{a_{e\tau}}_{\mu e}$, $P^{a_{\mu\tau}}_{\mu\mu}$ are the LIV-induced part of the probabilities, given as

$$P^{3\nu}_{\mu e} = 4s^2_{13}s^2_{23}\frac{\sin^2[(\hat{A}-1)\Delta]}{(\hat{A}-1)^2} + 2\alpha s_{13}\sin 2\theta_{12}\sin 2\theta_{23}\frac{\sin[\hat{A}\Delta]}{\hat{A}} \times \frac{\sin[(\hat{A}-1)\Delta]}{\hat{A}-1}\cos(\Delta+\delta_{13}) \tag{8}$$

$$P^{3\nu}_{\mu\mu} = 1 - \sin^2 2\theta_{23}\sin^2\Delta \tag{9}$$

$$P^{a_{e\mu}}_{\mu e} \simeq \frac{4|a_{e\mu}|\hat{A}\Delta s_{13}\sin 2\theta_{23}\sin\Delta}{\sqrt{2}G_F N_e}[Z_{e\mu}\sin(\delta_{13}+\phi_{e\mu}) + W_{e\mu}\cos(\delta_{13}+\phi_{e\mu})] \tag{10}$$

$$P^{a_{e\tau}}_{\mu e} \simeq \frac{4|a_{e\tau}|\hat{A}\Delta s_{13}\sin 2\theta_{23}\sin\Delta}{\sqrt{2}G_F N_e}[Z_{e\tau}\sin(\delta_{13}+\phi_{e\tau}) + W_{e\tau}\cos(\delta_{13}+\phi_{e\tau})] \tag{11}$$

$$P^{a_{\mu\tau}}_{\mu\mu} = \frac{4|a_{\mu\tau}|\hat{A}\Delta\sin 2\theta_{23}\sin\Delta}{\sqrt{2}G_F N_e} \times [Z_{\mu\tau}\cos\phi_{\mu\tau} + W_{\mu\tau}\cos\phi_{\mu\tau}] \tag{12}$$

where $\Delta = \frac{\Delta_{31}L}{4E}$, $\alpha = \Delta_{21}/\Delta_{31}$, $\hat{A} = \frac{2\sqrt{2}G_F N_e E}{\Delta_{31}}$, $A = 2\sqrt{2}G_F N_e E$, $s_{ij} = \sin\theta_{ij}$, $c_{ij} = \cos\theta_{ij}$,

$$\begin{aligned} Z_{e\mu} &= -\cos\theta_{23}\sin\Delta, \\ Z_{e\tau} &= \sin\theta_{23}\sin\Delta, \\ Z_{\mu\tau} &= -\sin^2 2\theta_{23}\cos\Delta \end{aligned} \tag{13}$$

$$\begin{aligned} W_{e\mu} &= c_{23}\left(\frac{s^2_{23}\sin\Delta}{\Delta.c^2_{23}} + \cos\Delta\right), \\ W_{e\tau} &= s_{23}\left(\frac{\sin\Delta}{\Delta} - \cos\Delta\right), \\ W_{\mu\tau} &= \frac{-\cos^2 2\theta_{23}\sin\Delta}{\Delta} \end{aligned} \tag{14}$$

3.1 Variation in $P_{\mu e}$ with phases at fixed $a_{e\mu}, a_{e\tau}, a_{\mu\tau}$

In the presence of the LIV parameters, the appearance channel probability depends on the parameters $a_{e\mu}$, $a_{e\tau}$, and $a_{\mu\tau}$. It also depends on the LIV phases $\phi_{e\mu}$, and $\phi_{e\tau}$ in conjunction with δ_{13}. The modifications in $P_{\mu e}$ due to LIV parameters are probed in this section at baselines of 1100 km and 295 km. In the plots that follow, the values of the oscillation parameters are chosen as [41], $\theta_{12} = 33.44°$, $\theta_{13} = 8.57°$, $\theta_{23} = 49°$, $\Delta_{21} = 7.42 \times 10^{-5}$ eV^2, and $|\Delta_{31}| = 2.515 \times 10^{-3}$ eV^2. $P_{\mu e}$ is plotted as a function of δ_{13} at 0.6 GeV in Fig. 1 for normal (top panel) and inverted (bottom panel) mass orderings for baselines of 295 km (red) and 1100 km (blue), while the values of the non-diagonal LIV parameters are kept fixed at 10^{-23} GeV. The bands refer to the variation of LIV phases. The significant points to be noted are as follows:

- It can be observed from both top and bottom panels that the effect of $\phi_{e\mu}$, $\phi_{e\tau}$ is larger than $\phi_{\mu\tau}$, as the width of the red and blue bands is narrower in the right panels than in the left and middle ones. This can be understood from Eqs. (10) and (11), as $P_{\mu e}$ has no contribution from $\phi_{\mu\tau}$ at the leading order, as seen in [40]. In our numerical plots, however, we observe very weak dependence on $\phi_{\mu\tau}$, and the same can be found in the analytical expressions derived in [42].

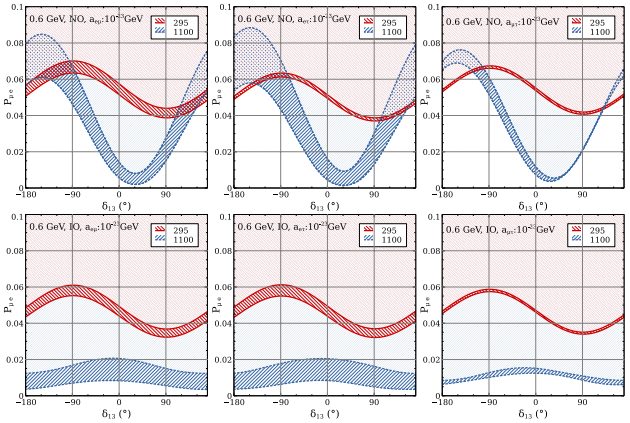

Fig. 1 $P_{\mu e}$ as a function of δ_{13} for NO (top) and IO (bottom) at 0.6 GeV. The plots shown in the left, middle, and right panels are in the presence of $a_{e\mu} = 10^{-23}$ GeV, $a_{e\tau} = 10^{-23}$ GeV, and $a_{\mu\tau} = 10^{-23}$ GeV, respectively. The red and blue bands of probability corresponding to 295 km and 1100 km, respectively, signify variation of phases $\phi_{e\mu}$, $\phi_{e\tau}$, $\phi_{\mu\tau}$

- In the case of normal ordering (NO) (upper panels), the variation of $P_{\mu e}$ with δ_{13} for 1100 km is sharper, as 0.6 GeV is adjacent to the second oscillation maxima (0.7 GeV). However, at 295 km, the variation is smaller because the first oscillation maxima occurs at 0.6 GeV. Thus, probabilities at CP-conserving values $0°, \pm 180°$ are more separated from probabilities at other CP-violating values at 1100 km than at 295 km.
- Also, in the case of NO, the maxima and minima of $P_{\mu e}$ occur at different δ_{13} values for 295 km and 1100 km, leading to different CP sensitivity at different channels. For instance, the probabilities at $\delta_{13} = \pm 90°$ values for 295 km are the most different from the probabilities at CP-conserving $\delta_{13} = 180°, 0°$. Therefore, CP sensitivity will be greatest at $\delta_{13} = \pm 90°$ at 295 km. However, in the case of 1100 km, the probabilities at $\delta_{13} = \pm 90°$ are very close to probability values at $\pm 180°$. Therefore, while evaluating the sensitivity to CP discovery at $\delta_{13} = \pm 90°$, there will be higher sensitivity for the 295 km +1100 km configuration than the individual 295 km and 1100 km due to the synergy.
- For inverted ordering (IO), the variation with δ_{13} is very flat at 1100 km, while the variation at 295 km remains similar to NO. This leads to poor sensitivity for CP discovery for the T2HKK configuration for IO.

The disappearance probability $P_{\mu\mu}$ does not depend on the CP phase at the leading order. Therefore, in the case of $P_{\mu\mu}$, dependence on $\phi_{\mu\tau}$ is not linked with δ_{13}.

In Fig. 2, the oscillation probabilities $P_{\mu e}$ and $P_{\bar{\mu}\bar{e}}$ are plotted as a function of δ_{13} at fixed energy of 0.6 GeV corresponding to 295 km and 1100 km baselines for NO and IO

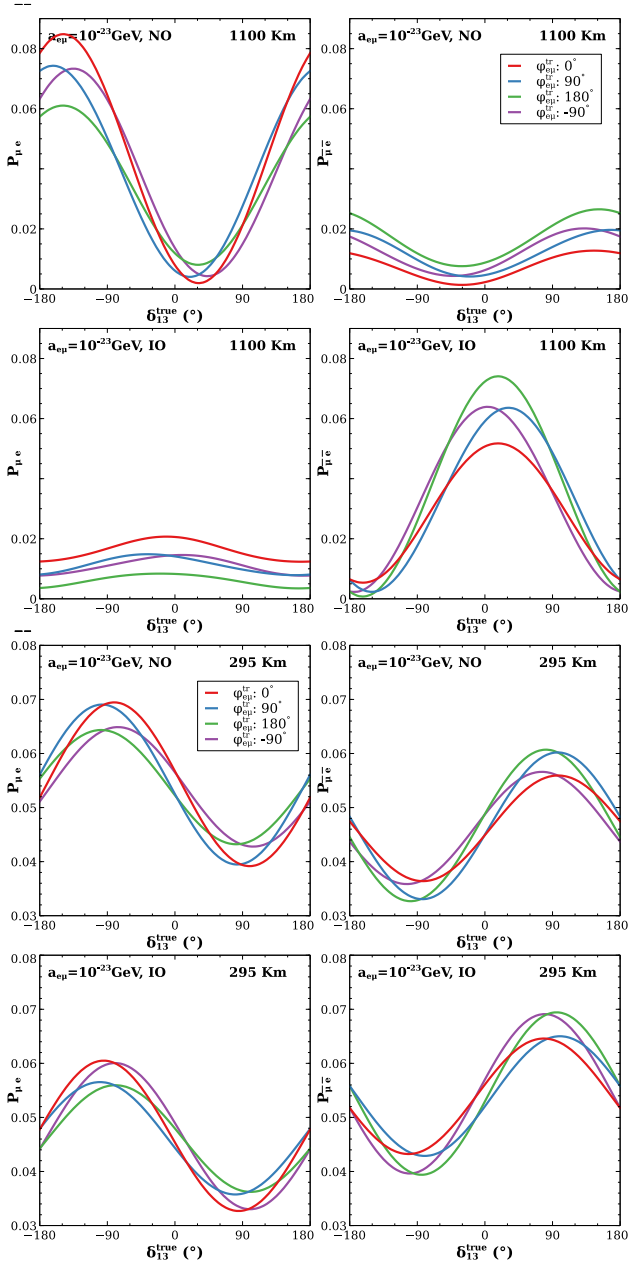

Fig. 2 $P_{\mu e}$ (left) and $P_{\bar{\mu}\bar{e}}$ (right) as a function of δ_{13}^{true} for true values of $\theta_{23} = 49°$ and $a_{e\mu} = 10^{-23}$ GeV. The panels on the top (bottom) two rows refer to 295 km (1100 km) for NO (top) and IO (bottom). Violet, red, green, and blue refer to $\phi_{e\mu}^{true} = -90°, 0°, 90°, 180°$, respectively

considering $\theta_{23} = 49°$ and $a_{e\mu} = 10^{-23}$ GeV. We observe the following features:

- At 1100 km, the $P_{\mu e}$ probabilities have larger values than $P_{\bar{\mu}\bar{e}}$ in NO. However, that order reverses in IO.
- In NO, the $P_{\mu e}$ curves show a peak at the lower half plane (LHP) $[-180° : 0°]$ in the range $-160° : -130°$. The peaks of $P_{\bar{\mu}\bar{e}}$ curves occur at the upper half plane (UHP) $[0° : 180°]$ in the range $130° : 170°$.

- In the case of IO for 1100 km, both the $P_{\mu e}$ and $P_{\bar{\mu}\bar{e}}$ have maxima around 0°.
- At 295 km, various probabilities for different values of $\phi_{e\mu}$ vary over a small region while being very close to each other.
- At 295 km, the maxima of $P_{\mu e}$ and $P_{\bar{\mu}\bar{e}}$ curves occur around ±90° for both NO and IO.
- In the case of both 295 km and 1100 km, the red (green) curves corresponding to $\phi^{tr}_{e\mu} = 0°(180°)$ give the maximum (minimum) variation in $P_{\mu e}$. In $P_{\bar{\mu}\bar{e}}$, this order is reversed.

4 χ^2 analysis of CP discovery

In this section, we study the potential of the T2HKK/T2HK experiments for CP discovery. The configurations for the proposed experiments are as follows: (i) T2HK, with two detectors of 187 kton at 295 km, and (ii) T2HKK, with one detector of 187 kton at 295 km and another similar detector at 1100 km away in Korea [43]. For our study, we consider the first detector and the second detector of T2HKK at an off-axis angle of 2.5° and 1.5°, respectively, from the source at the J-PARC facility in Tokai [33]. T2HKK offers us the advantage of a larger matter effect at 1100 km than T2HK. For our numerical analysis with GLoBES [44,45], we use a proposed beam with energy of 1.3 MW considering 2.5 years of neutrino mode and 7.5 years of anti-neutrino mode run time with an exposure of 27×10^{21} proton on target (POT). The detector configurations and systematic errors are taken from [33] and are tabulated in Table 2.

The final value of χ^2 is derived after marginalization over pull variables ξ and variables of oscillation ω as follows:

$$\Delta\chi^2 = \text{Min}[\chi^2_{\text{stat}}(\omega,\xi) + \chi^2_{\text{pull}}(\xi)], \tag{15}$$

where χ^2_{pull} includes the symmetric errors, and the Poissonian χ^2_{stat} is defined as

$$\chi^2_{\text{stat}}(\omega,\xi) = 2\sum_i \left[N_i^{test} - N_i^{true} + N_i^{true}\ln\frac{N_i^{true}}{N_i^{test}}\right] \tag{16}$$

$$\chi^2_{\text{pull}} = \sum_{r=1}^{4}\xi_r^2, \tag{17}$$

where N_i^{true} is the total true no of events, and N_i^{test} is the events generated by a theoretical model in the ith energy beam. The events are calculated as

$$N_i^{test}(\omega,\xi) = \sum_{k=s,b}\left[N_i^k(\omega)\left(1 + c_i^{k,norm}\xi^{k,norm} + c_i^{k,tilt}\xi^{k,tilt} \times \frac{2E_i - E_{max} - E_{min}}{2(E_{\max} - E_{\min})}\right)\right] \tag{18}$$

Table 2 True values of all the parameters and their range of marginalization

Parameter	True value	Marginalization range
θ_{12}	33.4°	N.A.
θ_{13}	8.62°	N.A.
θ_{23}	49°	(39°, 51°)
δ_{13}	(−180°, 180°)	0°, 180°
Δ_{21}	7.4×10^{-5} eV^2	N.A.
$\lvert\Delta_{31}\rvert$	2.5×10^{-3} eV^2	$(2.4, 2.6) \times 10^{-3}$ eV^2
$a_{\alpha\beta}$	10^{-23} GeV	$(10^{-22}, 10^{-24})$ GeV
$\phi_{\alpha\beta}$	(−180°, 180°)	0°, 180°

Table 3 The signal (background) normalization uncertainties of the experiments for different channels

Channel	295 km	1100 km
ν_e appearance	3.2% (5%)	3.8% (5%)
ν_μ disappearance	3.6% (5%)	3.8% (5%)
$\bar{\nu}_e$ appearance	3.9% (5%)	4.1% (5%)
$\bar{\nu}_\mu$ disappearance	3.6% (5%)	3.8% (5%)

The systematic uncertainties are included through the method of pull in terms of the variables of signal normalization error, background normalization error, energy calibration error on signal, and background (tilt). In this work, the test parameters ω are $\theta_{23}, \delta_{13}, |\Delta_{31}|, a_{\alpha\beta}, \phi_{\alpha\beta}$.

We have seen in Table 1 that the current bound for NSI parameters is $\sim 10^{-23}$ GeV. Therefore, we have considered true values of $a_{e\mu}, a_{e\tau}, a_{\mu\tau} = 10^{-23}$ GeV throughout our study. For numerical analysis for CP discovery in the standard case, the test values are considered as $\delta_{13} = 0°, 180°$. In the presence of an extra LIV phase, the CP-conserving test values of $\delta_{13}, \phi_{\alpha\beta}$ correspond to the four combinations (0°, 0°), (0°, 180°), (180°, 0°), (180°, 180°). While performing chi-square(χ^2) analysis in the presence of LIV, we consider one parameter to be nonzero at a time. Apart from phases, we have marginalized the chi square over θ_{23} and $|\Delta_{31}|$. The true values [1] and the marginalization ranges of the parameters are given in Table 3. The run time in neutrino and anti-neutrino mode is 2.5 years and 7.5 years, respectively.

4.1 Single detector analysis

In this section, the sensitivity to CP discovery is probed with a single detector at 295 km and 1100 km. This helps in understanding the features of these individual baselines. The total event rates get equal contributions from neutrinos and anti-neutrinos because of the chosen run time. Therefore, studying sensitivity for individual channels will help in understanding

the total sensitivity. In this section, we study the effect of only the LIV parameter $a_{e\mu}$ as a representative case.

The χ^2 corresponding to 1100 km in ν_e, $\bar{\nu}_e$, neutrino ($\nu_e + \nu_\mu$), anti-neutrino channels ($\bar{\nu}_e + \bar{\nu}_\mu$), and the total χ^2 is plotted from the first to fifth row, respectively, in the panels of Fig. 3. The left(right) panels correspond to the NO (IO). The different true values of $\phi_{e\mu} = -90°, 0°, 90°, 180°$ are shown by violet, red, blue, and green curves, respectively. The features of significance in Fig. 3 are as follows:

- In the ν_e mode (NO), the red curve $\phi_{e\mu} = 0°$ has the maximum sensitivity in both half-planes, but in the LHP, the magnitude at the peak is significantly larger. The green curve $\phi_{e\mu} = 180°$ has the lowest sensitivity. This is consistent with the features seen from the plot of $P_{\mu e}$ in the left panels of Fig. 2.
- In the $\bar{\nu}_e$ mode (NO), the highest sensitivity is achieved for the green $\phi_{e\mu} = -90°$ and blue curve $\phi_{e\mu} = 180°$ in both UHP and LHP, but the peak value in UHP is higher.
- Note that in the neutrino (anti-neutrino) channel shown in the third (fourth) row, the sensitivities increase significantly due to the inclusion of $\nu_\mu(\bar{\nu}_\mu)$. This is due to the synergy between electron and muon channels, further addressed in Fig. 5.
- In the case of total sensitivity (NO), the red curve ($\phi_{e\mu} = 0°$) has the highest sensitivity in the UHP, and the blue curve ($\phi_{e\mu} = 180°$) reaches the maximum sensitivity in the LHP. While marginalizing, the minimum of χ^2 occurs at different test values of the parameters for neutrino and anti-neutrino mode, leading to a synergistic effect. The overall sensitivity is enhanced due to this synergy.
- In the case of ν_e mode for IO, the red (green) shows the maximum (minimum) sensitivity, and the value of χ^2 is higher in the UHP than LHP. Here, the sensitivities are lower than the NO case that can be justified by low variation of $P_{\mu e}$ plots in Fig. 2.
- In the context of ν_e mode for IO, the green (red) curve reaches the maximum (minimum) value of χ^2. The green curve's maximum value of χ^2 is predominantly the highest in the UHP. The other curves also have maxima of higher value in the UHP.
- Similar to NO, we also observe synergistic effects in neutrino (anti-neutrino) mode in the form of overall increased sensitivity.
- In the case of IO for the total sensitivity, the green curve ($\phi_{e\mu} = 0°$) has the maximum χ^2 in the LHP and UHP with the latter case having a significantly higher value.
- It is to be noted that the sensitivity curves for $\phi_{e\mu}^{true} = -90°, 90°$ show nonzero sensitivity at $\delta_{13}^{true} = 0°, \pm 180°$ as the true values of $\phi_{e\mu}$ are CP-non-conserving.

In Fig. 4, the value of χ^2 is depicted as a function of δ_{13}^{true} for a single detector at 295 km considering true ordering as

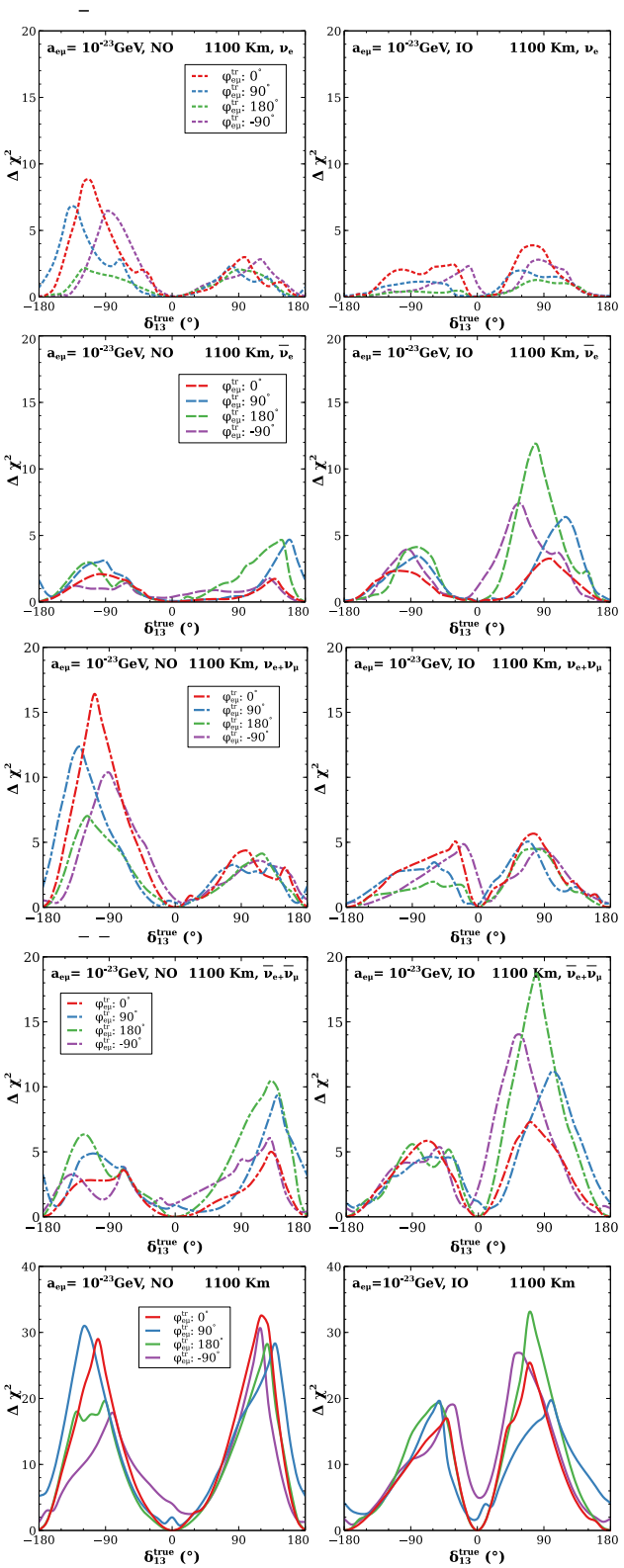

Fig. 3 χ^2 in ν_e (first), $\bar{\nu}_e$ (second), $\nu_e + \nu_\mu$ (third), $\bar{\nu}_e + \bar{\nu}_\mu$ (fourth) channel, and total χ^2 (bottom) as a function of δ_{13}^{true} for true values of $\theta_{23} = 49°$ with $a_{e\mu} = 10^{-23}$ GeV at 1100 km for NO (left) and IO (right). Violet, red, green, and blue refer to $\phi_{e\mu} = -90°, 0°, 90°, 180°$, respectively

NO (left) and IO (right). The top, middle, and bottom panels refer to the sensitivity in neutrino, anti-neutrino, and the total sensitivity, respectively. The different colors for various $\phi_{e\mu}$ are similar to Fig. 3. The main observations of Fig. 4 are as follows:

- In NO and IO cases, in the ν_e mode, the red ($\phi_{e\mu} = 0°$) and green ($\phi_{e\mu} = 180°$) curves show the maximum and minimum sensitivity, respectively, in the LHP. However, in the UHP, all curves have similar very low sensitivity. In the $\bar{\nu_e}$ mode, the order of sensitivity for all the curves is almost the same in both the UHP and LHP.
- In both NO and IO, we observe higher sensitivity in neutrino mode. This is due to the fact that $P_{\mu e}$ curves have a higher range of variation than $P_{\bar{\mu}\bar{e}}$ curves, as was seen in Fig. 2.
- The addition of $\nu_\mu(\bar{\nu}_\mu)$ has led to a rise in the sensitivity in neutrino (anti-neutrino) mode, as seen from figures in the third (fourth) row.
- In the case of total sensitivity, all the curves have similar sensitivity, except for the red curve ($\phi^{tr}_{e\mu} = 0°$) showing a slightly higher value of χ^2 in the UHP.
- The total sensitivity is significantly higher than the sensitivity of ν_e and $\bar{\nu}_e$ channels. This is due to the synergy between the two channels, which is depicted in Fig. 5 where we plot the χ^2 as a function of θ^{test}_{23}.

The synergy between various channels in the test θ_{23} is depicted in Fig. 5 for 1100 km (right panel) and 295 km (left panel). It is observed that the shape of the total chi square is dictated by the ν_μ, $\bar{\nu}_\mu$ channels. Therefore, minima of the total sensitivity are obtained near the minima of the ν_μ, $\bar{\nu}_\mu$ channels with $\theta_{23} = 49°$ giving the lowest χ^2. Although, at the minima, the $\chi^2 \sim 0$ for ν_μ, $\bar{\nu}_\mu$ channels, the nonzero chi-square contribution from the ν_e, $\bar{\nu}_e$ channels boosts the chi square in neutrino ($\nu_e + \nu_\mu$) and anti-neutrino ($\bar{\nu}_e + \bar{\nu}_\mu$) mode, leading to enhanced total χ^2. Due to the opposite nature w.r.t θ^{test}_{23}, further synergy is observed between ν_e and $\bar{\nu}_e$ channels, elevating the total sensitivity.

4.2 Comparative analysis between T2HKK and T2HK

In this section, we compare and contrast the CP discovery potential of the proposed T2HKK and T2HK configurations. This study is performed for the LIV parameters $a_{e\mu}$, $a_{e\tau}$, $a_{\mu\tau}$ taking one of these to be nonzero at a time. In Fig. 6, we present the sensitivity as a function of δ^{true}_{13} for T2HKK (left) and T2HK (right) for NO (top) and IO(bottom) for $a^{true}_{e\mu} = 10^{-23}$ GeV. Different curves correspond to the different values of $\phi^{true}_{e\mu}$.

The major points observed from Fig. 6 are as follows:

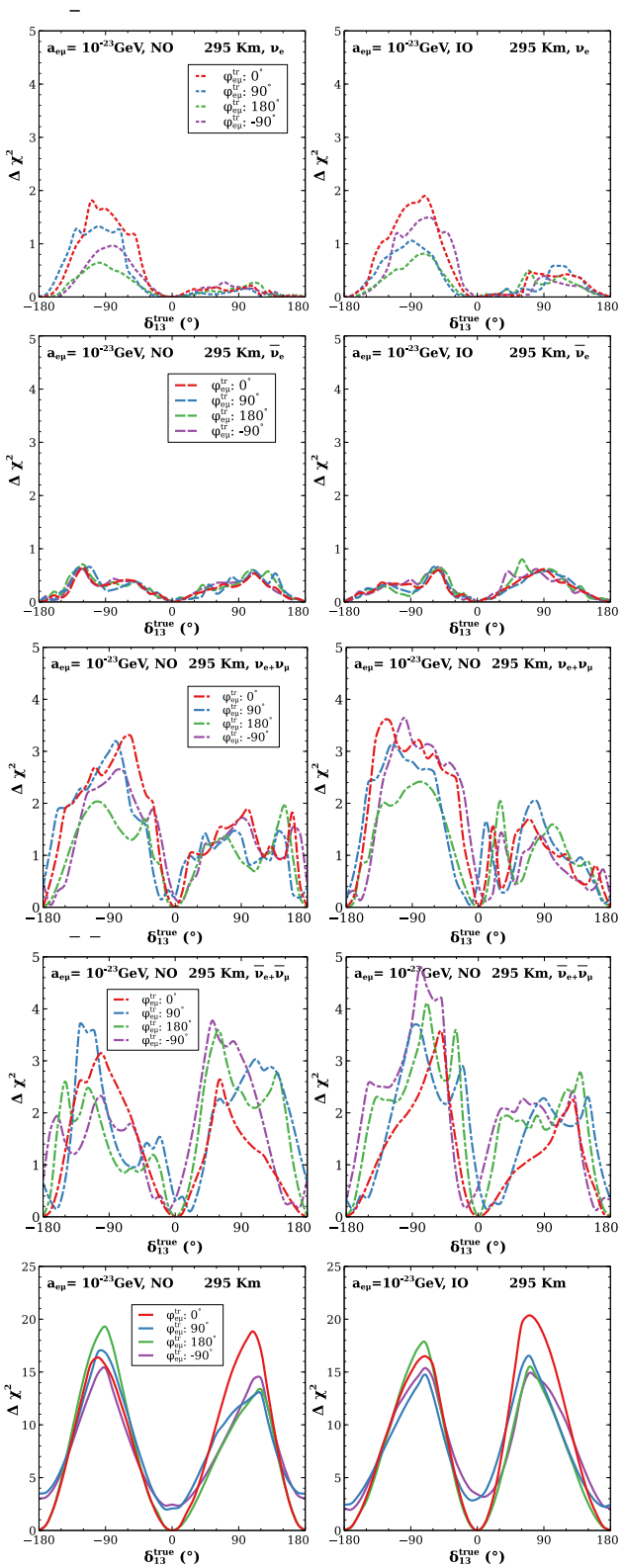

Fig. 4 χ^2 in ν_e (first), $\bar{\nu}_e$ (second), $\nu_e + \nu_\mu$ (third), $\bar{\nu}_e + \bar{\nu}_\mu$ (fourth) channel, and total χ^2 (bottom) as a function of δ^{true}_{13} for true values of $\theta_{23} = 49°$ with $a_{e\mu} = 10^{-23}$ GeV at 295 km for NO (left) and IO (right). Violet, red, green, and blue refer to $\phi_{e\mu} = -90°, 0°, 90°, 180°$, respectively

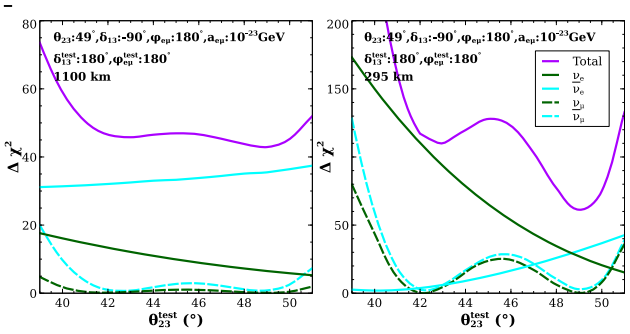

Fig. 5 χ^2 as a function of θ_{23}^{test} at 1100 km (left) and 295 km (right). Green (blue) refers to $\nu(\bar{\nu})$ channels, and violet gives total χ^2

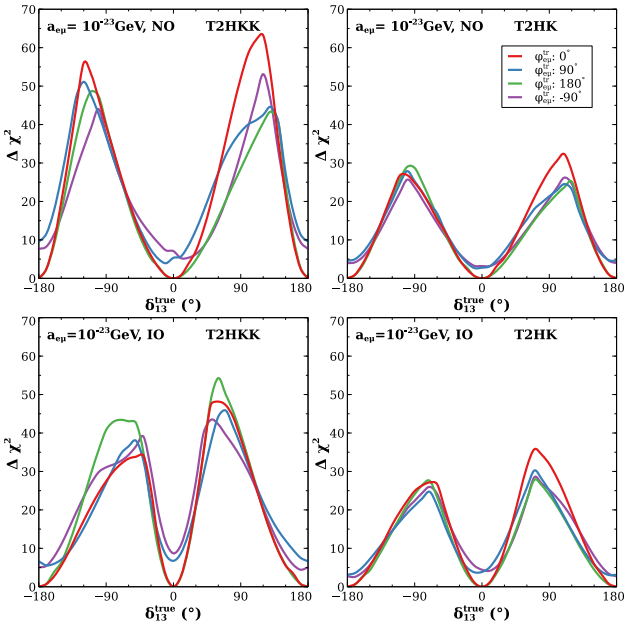

Fig. 6 χ^2 as a function of δ_{13}^{true} for true values of $\theta_{23} = 49°$ and $a_{e\mu} = 10^{-23}$ GeV in T2HKK (left) and T2HK (right) configurations for NO (top), and IO (bottom). Violet, red, green, and blue curves refer to $\phi_{e\mu}^{true} = -90°, 0°, 90°, 180°$ respectively

- T2HKK offers the best sensitivity for all values of the LIV phase $\phi_{e\mu}$. This is due to the synergistic effect between baselines of 1100 km and 295 km. This will be explained later in the context of Fig. 7.
- The highest sensitivity is obtained at $\delta_{13} = 90°$ for both T2HK and T2HKK. The corresponding values of $\phi_{e\mu}$ are 0° (180°) for NO(IO) case in T2HKK, and 0° in T2HK. This can be understood from Figs. 3 and 4, which show that for an individual baseline, the maxima comes at $\phi_{e\mu} = 0°$ around $\delta_{13} = 90°$.

In order to understand the synergy between baselines of 295 km and 1100 km in Fig. 7, we have shown the χ^2 as a function of test $a_{e\mu}$ (left) and θ_{23} (right) for a set of true parameters, keeping other test parameters fixed.

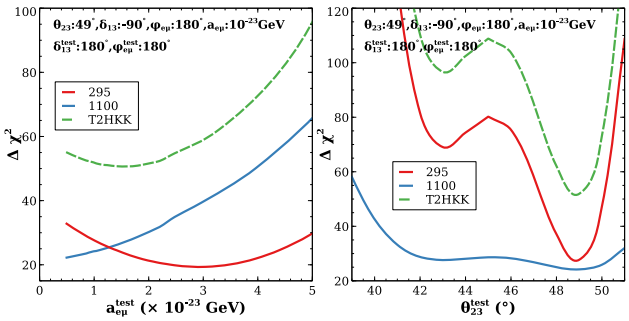

Fig. 7 χ^2 as a function of $a_{e\mu}^{test}$ (left) and θ_{23}^{test} (right) for true values of $\theta_{23} = 49°$, $\delta_{13} = -90°$, $\phi_{e\mu} = 180°$, and $a_{e\mu} = 10^{-23}$GeV

- From the left panel, we see that the minimum χ^2 for 295 km and 1100 km occurs at different test values of LIV parameter $a_{e\mu}$. Whereas in the case of T2HKK, the minimum occurs at a different test value of $a_{e\mu}$, thus enhancing the $\Delta\chi^2$ since both baselines contribute.
- In the right panel, the enhancement in χ^2 for T2HKK is due to the increased statistics. However, when marginalizing the χ^2 over other test parameters, the synergy is also observed in θ_{23}.

In Fig. 8, we present the values of χ^2 as a function of δ_{13}^{true} for $a_{e\tau}^{true} = 10^{-23}$ GeV in the T2HKK and T2HK configurations corresponding to NO (IO) in the top (bottom) column. The results are for the true values of phase $\phi_{e\tau}$ as $-90°$ (violet), 0° (red), 90° (blue), and 180° (green) using different colors as presented in the parentheses. The major observations are as follows:

- Similar to in Fig. 6, the sensitivity at T2HKK is quiet higher than T2HK configurations.
- We observe the maximum sensitivity in T2HKK around $\delta_{13} = 90°$ $(-90°)$, which is influenced by the maxima of $P_{\mu e}$ $(P_{\bar{\mu}\bar{e}})$ curves at 295 km occurring at 90° $(-90°)$. Although most of the curves show sensitivity in a similar range, the red $(\phi_{e\tau} = 0°)$ one reaches the highest at the UHP of δ_{13}^{true}.

We show the χ^2 as a function of true δ_{13} in Fig. 9 for effects of $a_{\mu\tau}$ for T2HKK and T2HK configurations in NO(top) and IO(bottom). The noteworthy points from these two figures are as follows:

- The best sensitivity is observed in T2HKK, but the sensitivity of T2HK is also very close. The reason behind this is no significant effect of $a_{\mu\tau}$ in $P_{\mu e}$.
- Also, there is very small variation of sensitivity w.r.t phase $\phi_{\mu\tau}$. This is due to the weak dependence of probabilities on $\phi_{\mu\tau}$ as seen in plots in Fig. 1.

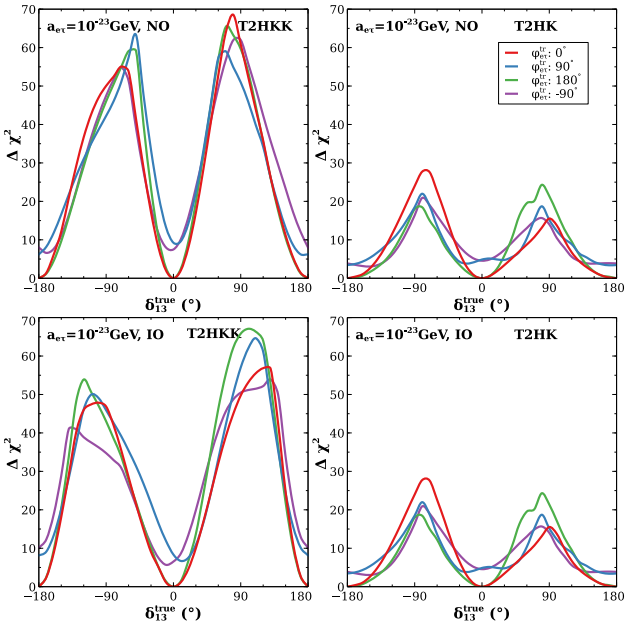

Fig. 8 χ^2 as a function of δ_{13}^{true} for true values of $\theta_{23} = 49°$ with $a_{e\tau} = 10^{-23}$ GeV for T2HKK (left) and T2HK (right) configurations in NO (top), and IO (bottom). Violet, red, green, and blue curves refer to $\phi_{e\mu}^{true} = -90°, 0°, 90°, 180°$, respectively

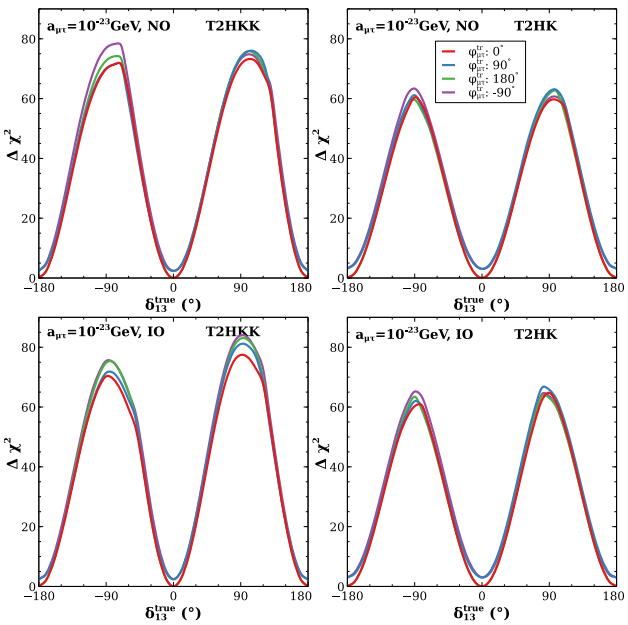

Fig. 9 χ^2 as a function of δ_{13}^{true} for true values of $\theta_{23} = 49°$ with $a_{\mu\tau} = 10^{-23}$ GeV for T2HKK (left) and T2HK (right) configurations for NO (top), and IO (bottom). Violet, red, green, and blue curves refer to $\phi_{\mu\tau}^{true} = -90°, 0°, 90°, 180°$, respectively

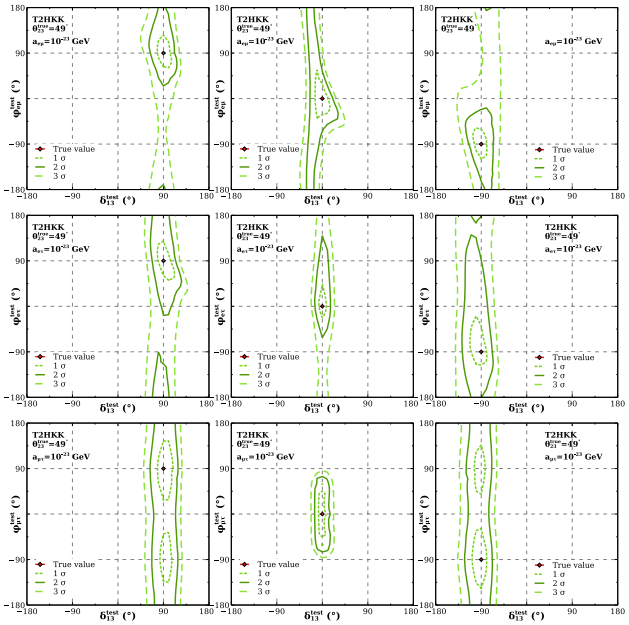

Fig. 10 1σ (dotted), 2σ (solid), and 3σ (dashed) contours [two degrees of freedom] corresponding to three different true values of δ_{13}, ϕ_{jk} for true LIV parameters $a_{e\mu}$ (top), $a_{e\tau}$ (middle), and $a_{\mu\tau}$ (bottom) having a value of 10^{-23} GeV for the T2HKK configuration

5 Precision χ^2 analysis of δ_{13}, $\phi_{\alpha\beta}$'s

In this section, we present the precision of δ_{13} and LIV phases $\phi_{\alpha\beta}$'s for T2HKK and T2HK in Figs. 10 and 11, respectively. These are presented in terms of contours in the $\phi_{\alpha\beta} - \delta_{13}$ test plane of various combinations of true values of $\phi_{\alpha\beta}$, $\delta_{CP} = 0°, 90°, -90°$. We consider the true values of LIV parameters as 10^{-23} GeV, $\theta_{23} = 49°$.

We can observe the following points from Fig. 10:

- In the topmost panels corresponding to $a_{e\mu}$, we observe closed 2σ contours for δ_{13}, $\phi_{e\mu} = 90°, -90°$ but not for δ_{13}, $\phi_{e\mu} = 0°$ (middle panel).
- On the other hand, in the middle panels corresponding to $a_{e\tau}$, the 2σ precision is better for δ_{13}, $\phi_{e\tau} = 0°$ but worse for $90°, -90°$
- In the lowest panel corresponding to $a_{\mu\tau}$, we observe that 2σ contours for $\delta_{13} = 90°$, $\phi_{\mu\tau} = 90°$ and $\delta_{13} = -90°$, $\phi_{\mu\tau} = -90°$ stretch over the full range of $\phi_{\mu\tau}$. However, in the middle panel, very good precision is obtained for $\delta_{13} = 0°$, $\phi_{\mu\tau} = 0°$ with a closed 3σ contour.
- The best sensitivity for $\phi_{e\mu}$ is seen for $\phi_{e\mu}^{tr} = 90°$, $\delta_{13}^{tr} = 90°$, whereas the best sensitivity for $\phi_{e\tau}$ is obtained at $\phi_{e\tau}^{tr} = 0°$, $\delta_{13}^{tr} = 0°$.

In Fig. 11, we plot similar contours for T2HK. We argue that the precision in δ_{13}, $\phi_{e\mu}$, and $\phi_{e\tau}$ is poorer for T2HK.

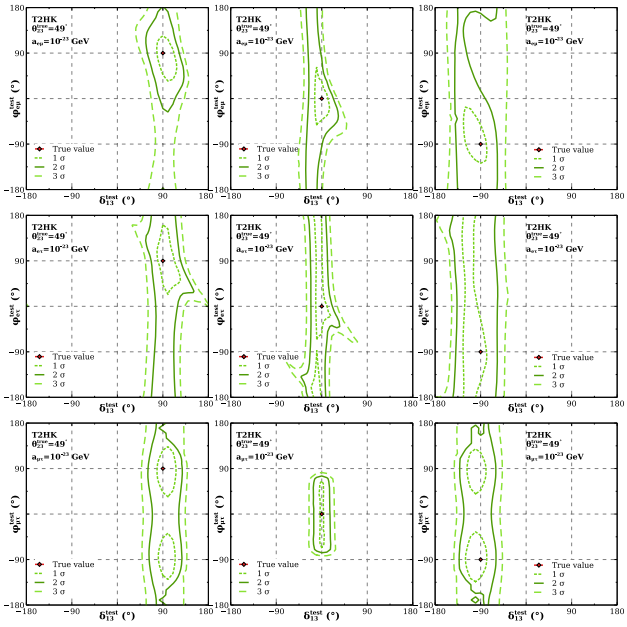

Fig. 11 1σ (dotted), 2σ (solid), and 3σ (dashed) contours [two degrees of freedom] corresponding to three different true values of δ_{13}, ϕ_{jk} for true LIV parameters $a_{e\mu}$ (top), $a_{e\tau}$ (middle), and $a_{\mu\tau}$ (bottom) having a value of 10^{-23} GeV for the T2HK configuration

This is expected since at 295 km, CP sensitivity is less. We can observe that the contours are similar for T2HK and T2HKK in the $\delta_{13} - \phi_{\mu\tau}$ plane, i.e., precision is similar in both configurations, as also seen in Fig. 9. The best sensitivity is obtained in T2HK also for $\delta_{13} = 0°$, $\phi_{\mu\tau} = 0°$.

6 Discussion

The main focus of our work is to investigate the CP sensitivity in the future T2HK/T2HKK experiment in the presence of the CPT-violating LIV parameters. We first study the CP discovery potential for individual baselines of 295 km and 1100 km in the presence of LIV phases and ascertain the role of neutrino and anti-neutrino contributions to the total χ^2. We found that at a fixed baseline, the sensitivity increases due to synergy between the electron and muon channels as well as between the neutrino and anti-neutrino channels. Then we obtain the sensitivity for T2HK and T2HKK configurations. We find that T2HKK gives a better sensitivity because of the synergistic effects of 295 km and 1100 km for LIV in the $e-\mu$ and $e-\tau$ sectors. We have identified synergy in parameters of $a_{\alpha\beta}, \theta_{23}, \phi_{\alpha\beta}, \delta_{13}$. However, for LIV in the $\mu-\tau$ sector, both configurations give similar sensitivity. This is because of the weak dependence of $P_{\mu e}$ on $\phi_{\mu\tau}$.

We also obtain the precision of δ_{CP}, $\phi_{\alpha\beta}$ for various true values of these phases in T2HK and T2HKK. We have found that the sensitivity of δ_{13} is better for the T2HKK configuration in the presence of $a_{e\mu}, a_{e\tau}$. In the case of $a_{\mu\tau}$, the sensitivity is best for $\delta_{13} = 0°$, $\phi_{\mu\tau} = 0°$.

Acknowledgements SG acknowledges the J. C. Bose Fellowship (JCB/2020/000011) of the Science and Engineering Research Board of the Department of Science and Technology, Government of India.

Data Availability Statement This manuscript has no associated data or the data will not be deposited. [Authors' comment: We have generated plots using data simulated using GLoBES and the detector configuration and values of parameters used are given in Sect. 4. Anyone can generate the data and plots using the given specifications.]

Funded by SCOAP[3].

References

1. I. Esteban, M.C. Gonzalez-Garcia, M. Maltoni, T. Schwetz, A. Zhou, JHEP **09**, 178 (2020). https://doi.org/10.1007/JHEP09(2020)178. arXiv:2007.14792 [hep-ph]
2. V.A. Kostelecky, S. Samuel, Phys. Rev. D **39**, 683 (1989). https://doi.org/10.1103/PhysRevD.39.683
3. V.A. Kostelecky, S. Samuel, Phys. Rev. Lett. **63**, 224 (1989). https://doi.org/10.1103/PhysRevLett.63.224
4. V.A. Kostelecky, S. Samuel, Phys. Rev. D **40**, 1886 (1989). https://doi.org/10.1103/PhysRevD.40.1886
5. V.A. Kostelecky, S. Samuel, Phys. Rev. Lett. **66**, 1811 (1991). https://doi.org/10.1103/PhysRevLett.66.1811
6. D. Colladay, V.A. Kostelecky, Phys. Rev. D **55**, 6760 (1997). https://doi.org/10.1103/PhysRevD.55.6760. arXiv:hep-ph/9703464
7. V.A. Kostelecký, R. Potting, Phys. Lett. B **381**, 89 (1996). https://doi.org/10.1016/0370-2693(96)00589-8
8. V.A.Kostelecky, R. Potting, Nucl. Phys. B **359**, 545 (1991). https://doi.org/10.1016/0550-3213(91)90071-5
9. V.A. Kostelecky, R. Potting, Phys. Rev. D **51**, 3923 (1995). https://doi.org/10.1103/PhysRevD.51.3923. arXiv:hep-ph/9501341
10. D. Colladay, V.A. Kostelecky, Phys. Lett. B **344**, 259 (1995). https://doi.org/10.1016/0370-2693(94)01600-H. arXiv:hep-ph/9501372
11. D. Colladay, V.A. Kostelecky, Phys. Rev. D **52**, 6224 (1995). https://doi.org/10.1103/PhysRevD.52.6224. arXiv:hep-ph/9510365
12. Y. Abe et al. (Double Chooz), Phys. Rev. D **86**, 112009 (2012). https://doi.org/10.1103/PhysRevD.86.112009. arXiv:1209.5810 [hep-ex]
13. A.A. Aguilar-Arevalo et al. (MiniBooNE), Phys. Lett. B **718**, 1303 (2013). https://doi.org/10.1016/j.physletb.2012.12.020. arXiv:1109.3480 [hep-ex]
14. P. Adamson et al. (MINOS), Phys. Rev. Lett. **101**, 151601 (2008). https://doi.org/10.1103/PhysRevLett.101.151601. arXiv:0806.4945 [hep-ex]

15. P. Adamson et al. (MINOS), Phys. Rev. Lett. **105**, 151601 (2010). https://doi.org/10.1103/PhysRevLett.105.151601. arXiv:1007.2791 [hep-ex]
16. R. Abbasi et al. (IceCube), Phys. Rev. D **82**, 112003 (2010). https://doi.org/10.1103/PhysRevD.82.112003. arXiv:1010.4096 [astro-ph.HE]
17. L.B. Auerbach et al. (LSND), Phys. Rev. D **72**, 076004 (2005). https://doi.org/10.1103/PhysRevD.72.076004. arXiv:hep-ex/0506067
18. B. Aharmim et al. (SNO), Phys. Rev. D **98**, 112013 (2018). https://doi.org/10.1103/PhysRevD.98.112013. arXiv:1811.00166 [hep-ex]
19. Y. Huang, H. Li, B.-Q. Ma, Phys. Rev. D **99**, 123018 (2019). https://doi.org/10.1103/PhysRevD.99.123018. arXiv:1906.07329 [hep-ph]
20. D. Raikwal, S. Choubey, M. Ghosh. arXiv:2303.10892 [hep-ph] (2023)
21. U. Rahaman, Eur. Phys. J. C **81**, 792 (2021). https://doi.org/10.1140/epjc/s10052-021-09598-4. arXiv:2103.04576 [hep-ph]
22. R. Majhi, D.K. Singha, M. Ghosh, R. Mohanta, Phys. Rev. D **107**, 075036 (2023). https://doi.org/10.1103/PhysRevD.107.075036. arXiv:2212.07244 [hep-ph]
23. S. Sahoo, A. Kumar, S.K. Agarwalla, A. Dighe, Phys. Lett. B **841**, 137949 (2023). https://doi.org/10.1016/j.physletb.2023.137949
24. M. Aker et al. (KATRIN), Phys. Rev. D **107**, 082005 (2023). https://doi.org/10.1103/PhysRevD.107.082005. arXiv:2207.06326 [nucl-ex]
25. N. Fiza, N.R. Khan Chowdhury, M. Masud, JHEP **01**, 076 (2023). https://doi.org/10.1007/JHEP01(2023)076. arXiv:2206.14018 [hep-ph]
26. C. Li, B.-Q. Ma, Phys. Lett. B **835**, 137543 (2022). https://doi.org/10.1016/j.physletb.2022.137543. arXiv:2211.00900 [hep-ph]
27. B. Skrzypek, C.A. Argüelles. arXiv:2302.08998 [hep-ph] (2023)
28. C. Li, B.-Q. Ma, JHEP **03**, 230 (2023). https://doi.org/10.1007/JHEP03(2023)230. arXiv:2303.04765 [hep-ph]
29. S. Kumar Agarwalla, M. Masud, Eur. Phys. J. C **80**, 716 (2020). https://doi.org/10.1140/epjc/s10052-020-8303-1. arXiv:1912.13306 [hep-ph]
30. R. Majhi, S. Chembra, R. Mohanta, Eur. Phys. J. C **80**, 364 (2020). https://doi.org/10.1140/epjc/s10052-020-7963-1. arXiv:1907.09145 [hep-ph]
31. J.B. Albert et al. (EXO-200), Phys. Rev. D **93**, 072001 (2016). https://doi.org/10.1103/PhysRevD.93.072001. arXiv:1601.07266 [nucl-ex]
32. Hyper-Kamiokande. (2016)
33. K. Abe et al. (Hyper-Kamiokande), PTEP **2018**, 063C01 (2018), https://doi.org/10.1093/ptep/pty044. arXiv:1611.06118 [hep-ex]
34. D. Colladay, V.A. Kostelecký, Phys. Rev. D **55**, 6760 (1997). https://doi.org/10.1103/PhysRevD.55.6760
35. S. Sahoo, A. Kumar, S.K. Agarwalla, A. Dighe, Phys. Lett. B **841**, 137949 (2023). https://doi.org/10.1016/j.physletb.2023.137949. arXiv:2205.05134 [hep-ph]
36. K. Abe et al. (Super-Kamiokande), Phys. Rev. D **91**, 052003 (2015). https://doi.org/10.1103/PhysRevD.91.052003. arXiv:1410.4267 [hep-ex]
37. M.G. Aartsen et al. (IceCube), Nat. Phys. **14**, 961 (2018). https://doi.org/10.1038/s41567-018-0172-2. arXiv:1709.03434 [hep-ex]
38. K. Abe et al., Phys. Rev. D (2015). https://doi.org/10.1103/physrevd.91.052003
39. M. Masud, S. Roy, P. Mehta, Phys. Rev. D **99**, 115032 (2019). https://doi.org/10.1103/PhysRevD.99.115032. arXiv:1812.10290 [hep-ph]
40. J. Kopp, M. Lindner, T. Ota, J. Sato, Phys. Rev. D **77**, 013007 (2008). https://doi.org/10.1103/PhysRevD.77.013007. arXiv:0708.0152 [hep-ph]
41. I. Esteban, M. Gonzalez-Garcia, M. Maltoni, T. Schwetz, A. Zhou, J. High Energy Phys. (2020). https://doi.org/10.1007/jhep09(2020)178
42. M.E. Chaves, D.R. Gratieri, O.L.G. Peres, J. Phys. G **48**, 015001 (2020). https://doi.org/10.1088/1361-6471/abae17. arXiv:1810.04979 [hep-ph]
43. K. Hagiwara, N. Okamura, K.-I. Senda, Phys. Rev. D **76**, 093002 (2007). https://doi.org/10.1103/PhysRevD.76.093002. arXiv:hep-ph/0607255
44. P. Huber, M. Lindner, W. Winter, Comput. Phys. Commun. **167**, 195 (2005). https://doi.org/10.1016/j.cpc.2005.01.003. arXiv:hep-ph/0407333
45. P. Huber, J. Kopp, M. Lindner, M. Rolinec, W. Winter, Comput. Phys. Commun. **177**, 432 (2007). https://doi.org/10.1016/j.cpc.2007.05.004. arXiv:hep-ph/0701187